Nonlinear dependency of the bacterial flagellar motor speed on proton motive force and its consequences for swimming

Ekaterina Krasnopeeva [1,2*†], **Lucas Le Nagard**[2†], **Wilson Poon**[3], **Chien-Jung Lo**[4,5], **Teuta Pilizota**[2,6*]

[1] Institute of Science and Technology Austria, Am Campus 1, 3400 Klosterneuburg, Austria

[2] Centre for Synthetic and Systems Biology, King's Buildings, EH9 3FF, University of Edinburgh, Edinburgh, UK

[3] School of Physics and Astronomy, King's Buildings, EH9 3FD, University of Edinburgh, Edinburgh, UK

[4] Department of Physics and Center for Complex Systems, National Central University, Jhongli 32001, Taiwan

[5] Institute of Physics, Academia Sinica, Taipei 11529, Taiwan

[6] Department of Physics, Cavendish Laboratory, University of Cambridge, Cambridge, CB3 0HE, UK.

[†] These authors contributed equally to this work

[*] Corresponding authors

Abstract

The bacterial flagellar motor enables bacteria to swim by rotating helical flagellar filaments that form a bundle at the back of the cell. *Escherichia coli*'s motor uses the energy stored in the proton motive force (PMF) to generate the torque driving this rotation. Until now, motor speed was thought to be proportional to the PMF, irrespective of the viscous load. Here, we show that the PMF-speed proportionality saturates at high load and high PMF, and, thus, the PMF-speed relationship is nonlinear in the high torque regime. Furthermore, we show that free swimming occurs close to or within this saturated regime, making the observed limiting torque evolutionary relevant.

bacterial flagellar motor | proton motive force | torque | bacterial swimming

Correspondence: ***ekaterina.krasnopeeva@ista.ac.at, teuta.pilizota@ed.ac.uk***

Introduction

Many motile bacteria, such as *Escherichia coli* and *Salmonella enterica*, swim to search for favourable environments [1, 2, 3, 4, 5]. They use a bundle of rotating helical flagella, each driven by a bacterial flagellar motor (BFM). The BFM is a $\sim$45 nm in size nanomachine and one of only a few known examples of a biological rotary motors [6, 7, 8, 9, 10].

In the case of *E. coli*, the BFM consists of a rotor composed of the cytoplasmic and membranous/supramembranous rings, and of a stator made up of a varying number of $MotA_5MotB_2$ units [11, 12, 13, 14, 15]. Stator units produce the torque driving the motor rotation by allowing protons to cross the plasma membrane through MotB channels [6, 16]. This inward flux of protons is driven by the proton motive force (PMF), an electrochemical gradient of protons metabolically active cells maintain across their inner membrane [17, 18, 19, 20].

Within the stator, $MotA_5MotB_2$ pentamers dynamically bind/unbind from the motor and remain bound for typically 30 s before returning to a pool of $\sim$100 units floating in the membrane [21]. The average number of torque-generating units bound to the BFM increases with the motor torque, which is influenced by the magnitude of the PMF and by the viscous load attached to the motor [13, 14, 22]. The motor exhibits a characteristic torque-speed curve with a high-torque/low-speed plateau followed by a low-torque/high-speed regime [6, 23, 24, 25, 26].

Despite the above-mentioned mechanosensing characteristics, two seminal studies found that a remarkably simple relationship links the output of the motor to its driving force, the PMF [22, 27]. Those studies showed that the rotation speed of the BFM is proportional to the PMF across a range of PMF values, under both low and high viscous loads. A similar proportionality to the sodium motive force (SMF) was observed for sodium-powered motors, although the chemical and electrical components of the SMF had non-equivalent contributions at low sodium concentrations and at a low load [20, 28, 29, 30, 31].

While the previous work spans a set of PMF values [22], it does not cover the full physiological range that has been reported [32, 33]. Given that there must be a physical limit to the speed and torque that the BFM can deliver, it is interesting to enquire whether this limit could be reached in physiologically relevant conditions, and what the consequences of such a limit would be for bacterial swimming.

We therefore measured the rotational speed of the BFM across a wide range of physiologically achievable PMF values, increasing the PMF by providing a given amount of a carbon source or decreasing it with the addition of an ionophore, all while subjecting the motor to different viscous loads. By so exploring the entire PMF-torque space available to *E. coli* we find, contrary to previous thoughts, that the PMF-speed proportionality does not hold universally and

saturates at high PMF and high viscous load. We directly demonstrate that the relationship is limited by the maximum torque the motor can achieve. Moreover, we show that fully energised free-swimming cells experience this limit in aqueous environments, where small increases in viscosity result in a swimming speed that is independent of the PMF. Combining those results, we estimate the mechanical load under which the flagellar motors operate in free-swimming *E. coli*. Finally, we discuss our results in the context of previous work and explain apparent discrepancies.

Results

The linear relationship between BFM speed and PMF fails at high load. To probe the limits of the PMF-speed proportionality, we first recorded the speed of individual motors in the presence or absence of a carbon source. *E. coli* were grown in LB and washed in MM9 medium containing either 0 or 20 mM glucose, producing cells with moderate or high PMF, respectively. To record BFM speeds under different mechanical loads, we used the so-called bead assay [3, 6, 24], whereby we attach to the motor polystyrene spheres (beads) of various diameters (see *Materials and Methods*).

Contrary to expectations, the relative speed increase induced by glucose supplementation depended on bead sizes, Fig. 1A and SI Fig. 1. For the smaller loads ($0.35\,\mu\mathrm{m}$ and $0.5\,\mu\mathrm{m}$ beads), glucose addition induced a ~ 2-fold increase in BFM speed, while for higher loads ($1\,\mu\mathrm{m}$ and $1.5\,\mu\mathrm{m}$ beads) the speed increased by only 10-20%. Those differences indicate that the PMF-speed proportionality is not independent of the load.

To test whether this observation was specific to glucose and to probe motor speed variations in a wider PFM range, we exposed cells to butanol. Looking at the speed changes of motors loaded with $0.5\,\mu\mathrm{m}$ beads, we previously demonstrated that butanol behaves as an ionophore, collapsing *E. coli*'s PMF in a concentration-dependent manner [34]. Similarly, we exposed the cells washed in MM9+20 mM glucose (presumably reaching maximum PMF) to different concentrations of butanol (0-1%), while measuring the motor speed after butanol addition, but this time for different bead sizes.

Again, the relative changes in the BFM speed depended on the motor load, Fig. 1B, C, and SI Fig. 2. For $0.5\,\mu\mathrm{m}$ beads, the speed was inversely proportional to the butanol concentration, as before [34]. $0.35\,\mu\mathrm{m}$ beads behaved identically to $0.5\,\mu\mathrm{m}$ beads, Fig. 1B (*Inset*). In stark contrast, the speed of $1.5\,\mu\mathrm{m}$ beads remained constant for up to 0.25% butanol, a concentration at which the speed of $0.5\,\mu\mathrm{m}$ and $0.35\,\mu\mathrm{m}$ beads had already decreased by $\sim$60%, Fig. 1B. Comparing the results of five bead sizes, we found that the effect of butanol on motor speed gradually decreased as the load increased, starting from $0.75\,\mu\mathrm{m}$ beads, Fig. 1C. These results confirm that the proportionality between PMF and motor speed does not hold across different viscous loads.

To exclude the effect of cell-to-cell variability in their PMF and response to butanol, we simultaneously measured the speeds of two motors located on the same cell but operating under different viscous loads, similar to one of the previous experiments that demonstrated the linear relationship between motor speed and PMF [27]. We cultured the cells in the presence of sub-inhibitory concentrations of cephalexin, an antibiotic that induces filamentation in bacteria [35] (*Materials and Methods*). We attached a $0.5\,\mu\mathrm{m}$ bead to one motor, and a $1.5\,\mu\mathrm{m}$ bead to a different motor on the same bacterium, which was sufficiently elongated to ensure the absence of steric hindrance between the two beads, SI Video 1. We again treated those cells with a range of butanol concentrations (0-1%) in MM9+20 mM glucose, and found, consistently with our previous observations, that motor speeds were comparatively less sensitive to butanol treatment under high load, SI Videos 1 & 2. In particular, plotting the high-load ($1.5\,\mu\mathrm{m}$) speed as a function of the low-load ($0.5\,\mu\mathrm{m}$) speed for motors on the same cells clearly showed that the high-load speed saturates at higher PMF, Fig. 1D. In contrast, the speeds of two $0.5\,\mu\mathrm{m}$ beads attached to the same cell varied linearly, as expected for two motors driven by the same PMF in conditions where the PMF-speed proportionality holds. Taken together, our results show that the PMF-speed proportionality holds at low viscous loads but saturates at higher loads.

PMF-speed linearity is limited by the maximum torque. Since motor speed saturation occurred only at high load, we hypothesised that the PMF-speed proportionality is limited by the maximum torque that BFM can produce, $T_{\max}$. To test this, in Fig. 2 we replot the motor speed data of Fig. 1C as torque-PMF curves (see *Materials and Methods* for torque calculation). We converted butanol concentrations to relative PMF values by assuming that the BFM speed is proportional to the PMF for sufficiently low loads, that is, $0.35\,\mu\mathrm{m}$ and $0.5\,\mu\mathrm{m}$ beads whose speed response to butanol overlaps, SI Fig. 3. We further assign a relative value of 1 to the maximum PMF of our experiments, which was obtained in MM9+20 mM glucose at 0% butanol and is thus presumably close to the maximum physiological PMF.

The torque-PMF curves for the larger beads ($0.75\,\mu\mathrm{m}$, $1\,\mu\mathrm{m}$, and $1.5\,\mu\mathrm{m}$) all converge to the same torque at high PMF, Fig. 2A. We fitted those curves with an exponential function, $T = T_{\max}(1 - e^{-\frac{\mathrm{PMF}}{\mathrm{PMF_s}}})$, and found $T_{\max} \lesssim 1400\,\mathrm{pN\,nm}$. In Fig. 2B we show the individual torque-PMF curves recorded for all bead sizes, where we now fit the same exponential function but set $T_{\max}$ to $1400\,\mathrm{pN\,nm}$. For each viscous load, the fits returned $\mathrm{PMF_s}$, the relative PMF above which the torque-PMF relationship begins to saturate, Fig. 2C. For viscous loads characterised by $\mathrm{PMF_s}>1$, the saturation does not occur at physiological PMF and the BFM speed is proportional to PMF. For loads at which $\mathrm{PMF_s}<1$ the relationship is nonlinear; the motor speed is limited by the maximum torque and becomes insensitive to PMF for $\mathrm{PMF_s} < \mathrm{PMF}$.

Although we set $T_{\max}$ to $1400\,\mathrm{pN\,nm}$ in the fits of Fig. 2, we note that motor speeds and, thus, our estimates of the maximum torque varied somewhat between experiments. We discuss it in detail in *Supplementary Material*. Despite this variability in absolute numbers, the non-linearity of the PMF-speed relationship at high loads was consistently observed

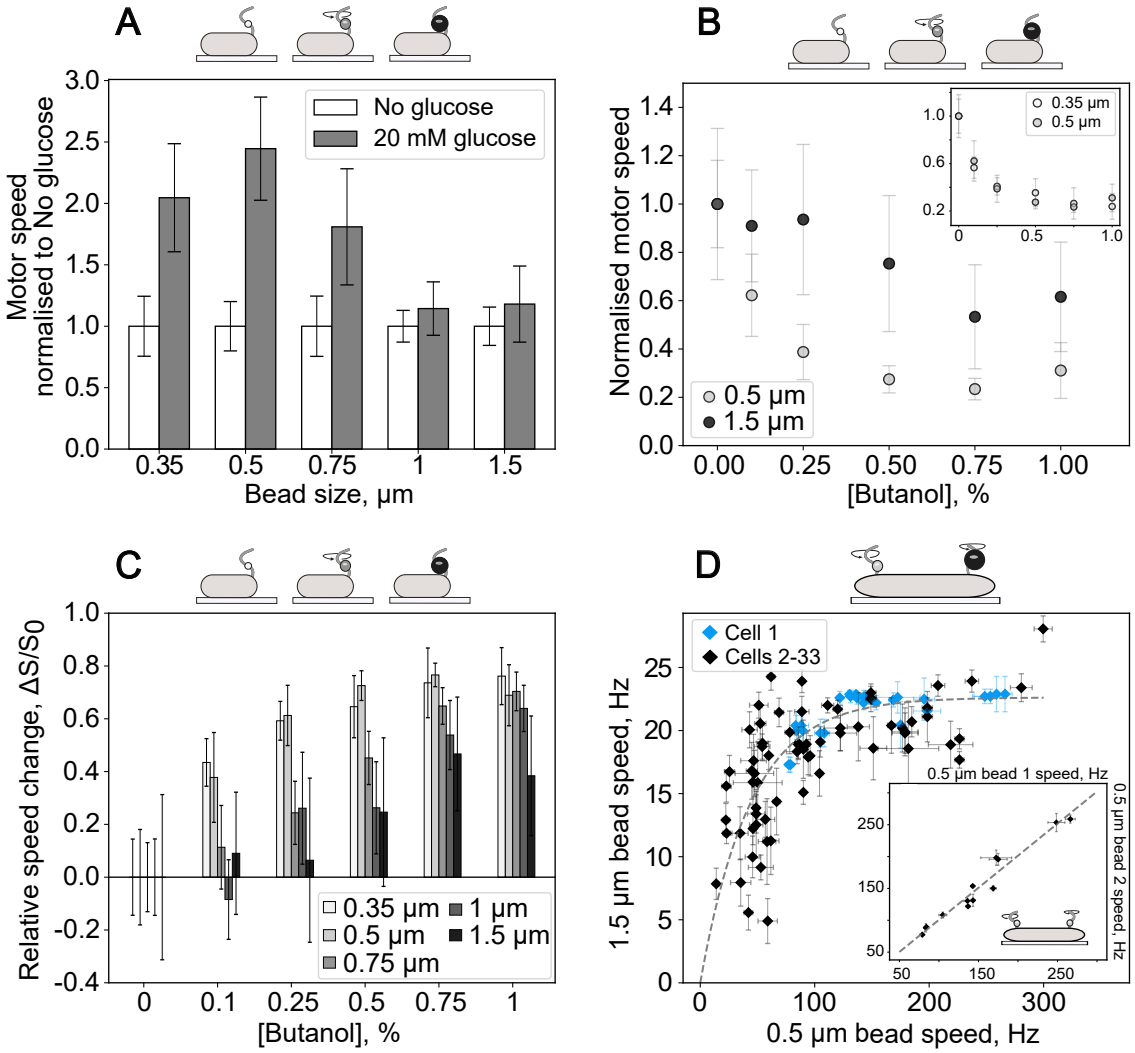

Fig. 1. Relative changes in flagellar motor speed at different PMFs depend on the viscous load on the motor. A. Relative increase in BFM speed upon glucose addition depends on the viscous load. Rotational frequencies of the BFM are measured with and without glucose, and normalised to the speeds with no glucose, for beads of different sizes ($0.35\,\mu\mathrm{m}$ to $1.5\,\mu\mathrm{m}$). Error bars are standard deviations for 22-37 cells per condition. Glucose addition induces a $\gtrsim 2$-fold speed increase for motors under low-load ($0.35\,\mu\mathrm{m}$, $0.5\,\mu\mathrm{m}$ beads), while those under high-load experience only a 20% speed increase. The top gives a cartoon of the bead assay, with different beads scaled to size between each other, but not with respect to the cell. **B.** Load-dependent relative decrease in BFM speed upon butanol addition. BFM speed under $0.5\,\mu\mathrm{m}$ and $1.5\,\mu\mathrm{m}$ beads load is measured at different butanol concentrations and normalised by the 0% butanol speed. The BFM speed stays constant up to 0.25% butanol addition under high load, where the low load motor speed is already reduced by 60%. (***Inset***) $0.35\,\mu\mathrm{m}$ and $0.5\,\mu\mathrm{m}$ beads display identical speed decays upon butanol addition. **C.** BFM speed sensitivity to butanol scales inversely with the load. The change in BFM speed, $\Delta S/S_0 = (S_0 - S)/S_0$, where S is the speed at a given butanol concentration and S_0 is the 0% butanol speed, is measured with beads of different sizes. Relative speed changes are less pronounced at higher loads for all concentrations. **D.** Speed of two motors under different loads on the same cell are not linearly proportional. For each cell, the frequencies of two motors, respectively loaded with a $0.5\,\mu\mathrm{m}$ and $1.5\,\mu\mathrm{m}$ bead, were recorded simultaneously while cells were treated with butanol. Most of the time one cell was treated with one or two butanol concentrations, where the blue points show the cell that was treated with more butanol concentrations. The data was collected for 33 double-bead cells. Dashed line: exponential fits applied to all the data. (***Inset***) A cell with two $0.5\,\mu\mathrm{m}$ beads attached shows linear proportionality between the speeds of the two motors. Dashed line: linear fit.

in all experiments, with calculated saturation torques ranging from $1252 \pm 150\,\mathrm{pN\,nm}$ to $1802 \pm 429\,\mathrm{pN\,nm}$, consistent with previous estimates for the limiting torque of the BFM [12, 24, 36]. All our observations thus demonstrate that the saturation of the PMF-speed proportionality is defined by the maximum torque that the motor can produce.

***E. coli* swim in the near-saturating regime.** We next asked whether *E. coli* can experience this saturation while swimming in aqueous media. Since saturation occurs at high mechanical loads, the answer depends on the load experienced by the BFM of swimming cells, for which a wide range of assumptions and estimates exist in the literature. Several studies report that the motors of swimming *E. coli* operate within or close to their low-speed, constant torque plateau [37, 38, 39], while others propose that they operate at much lower torque [40, 41, 42]. The first situation would make the swimming speed - PMF relationship prone to saturation, whereas in the second case the swimming speed should remain proportional to PMF. To answer our initial question and address conflicting reports, we measured the swimming speed of cells exposed to various butanol concentrations using differential dynamic microscopy (DDM) [43, 44, 45]. By comparing swimming speeds and motor speeds, each nor-

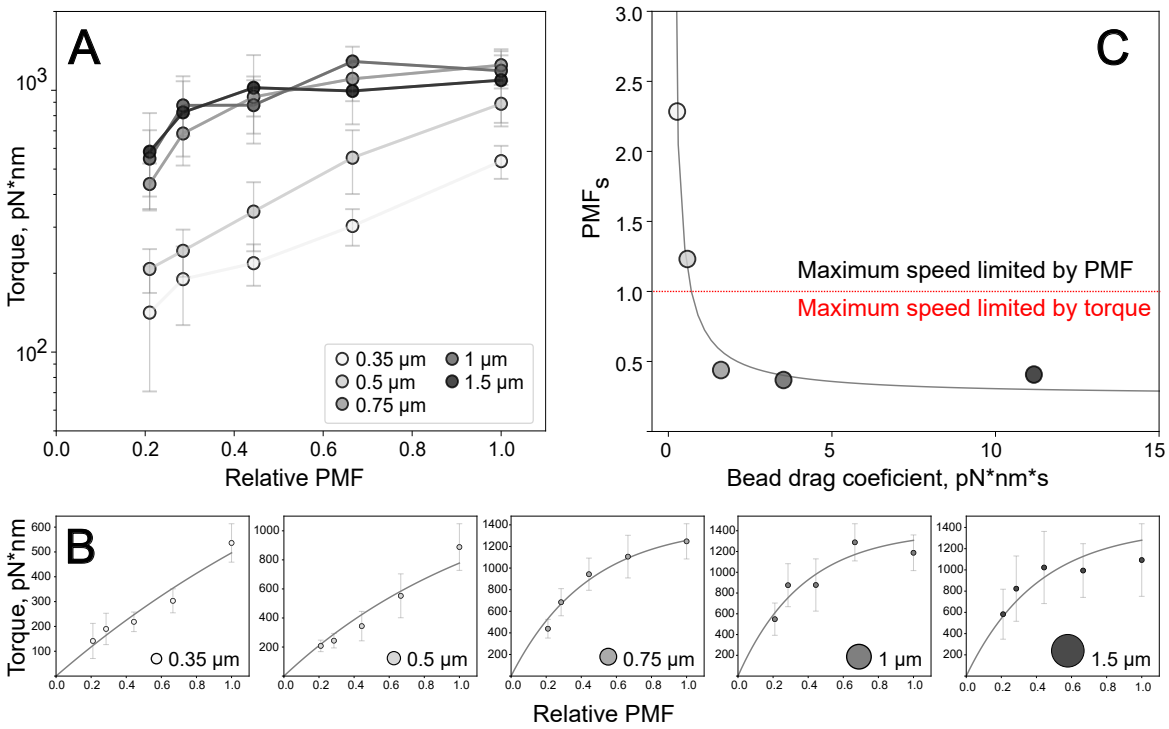

Fig. 2. BFM torque saturates at high viscous load and high PMF. A. BFM torque is plotted against relative PMF. Torque and relative PMF are calculated as described in *Materials and Methods*. The colour scale for beads of different sizes is given in the inset. For larger beads, the torque reaches the same saturating value, $T_{\max} \lesssim 1400\,\mathrm{pN\,nm}$, at high PMF. **B.** Individual Torque-PMF curves with exponential fits: $T = T_{\max}(1 - e^{-\frac{\mathrm{PMF}}{\mathrm{PMF_s}}})$, with T_{max} set to $1400\,\mathrm{pN\,nm}$. Cartoons of different bead sizes given in the bottom right corners are to scale and the same colour scale as in (A) is used. **C.** $\mathrm{PMF_s}$ is plotted against the drag coefficient of the beads, f_b, calculated as described in *Materials and Methods*. For loads with $\mathrm{PMF_s}$>1 ($0.35\,\mu\mathrm{m}$ and $0.5\,\mu\mathrm{m}$ beads), the maximum speed is not limited by torque for the whole range of physiological PMF values, whereas for loads with $\mathrm{PMF_s}$<1 the maximum speed is torque-limited and saturates at high PMF. The saturating PMF for each f_b can be estimated based on the fit.

malised by their respective value recorded in the absence of butanol, we found that the speed response curve of free-swimming cells lies between that of $0.5\,\mu\mathrm{m}$ and $0.75\,\mu\mathrm{m}$ beads, Fig. 3A. The butanol-speed curve for the free swimmers deviated slightly from the non-saturated 0.5 µm beads curve, indicating that the motors operate close to their saturating torque at maximum PMF. The addition of 8% Ficoll to the medium increased its viscosity ~ 3.5 fold (see *Methods* & *Supplementary Material*), consistent with previous measurements [23, 46]. The swimming speed response to butanol at this increased viscosity precisely matched the behaviour of 1 µm beads, Fig. 3B. Assuming the load with Ficoll to be equivalent to that of a $1\,\mu\mathrm{m}$ bead in Ficoll-free medium, and taking $\eta_{\mathrm{Ficoll}} = 3.5\eta$, we found that the motors of cells swimming in Ficoll-free medium operate under a load equivalent to a $0.6\,\mu\mathrm{m}$ bead (see *Supplementary Material*), in line with the results of Fig. 3A. As in the double bead experiment of Fig. 1D, high-load swimming speed in Ficoll exhibited saturation at high PMF compared to the low-load swimming speed, Fig. 3B (*Inset*).

Consistent with our hypothesis that the PMF-speed proportionality breaks at high PMF but holds at low PMF (below 45% of $\mathrm{PMF_{max}}$), normalising the swimming speeds obtained with and without Ficoll by their respective values at 0.25% butanol, equivalent to 44% $\mathrm{PMF_{max}}$, collapses the speed-butanol curves onto a single curve at low PMF, SI Fig. 4.

The motor torque-speed curves obtained in the butanol experiments allowed us to place swimming cells (in the absence of Ficoll) onto the torque-speed plane, Fig. 3C. Swimming in water (or other aqueous environments like MM9) happens just below or close to the "knee" of the torque-speed curves and reaches the limiting torque at the maximum PMF. Exponential fits of these experimental torque-speed curves are presented in SI Fig. 5.

Taken together, our results revise the well-known idealised torque-speed diagram, where the separation between individual torque-speed curves is proportional to the difference in PMF between them [25, 27]. The updated diagram includes the maximum torque, Fig. 3D, and the torque-speed curves now collapse on top of each other for higher PMF values. The lower limit of the viscous load experienced by free-swimming cells is estimated for an aqueous environment of viscosity similar to that of water. The swimming load line is expected to shift at a higher viscosity to the blue-shaded region in Fig. 3D.

Maximum torque in the context of previous work. Our results contradict previous measurements showing that the BFM speed and PMF are linearly proportional irrespective

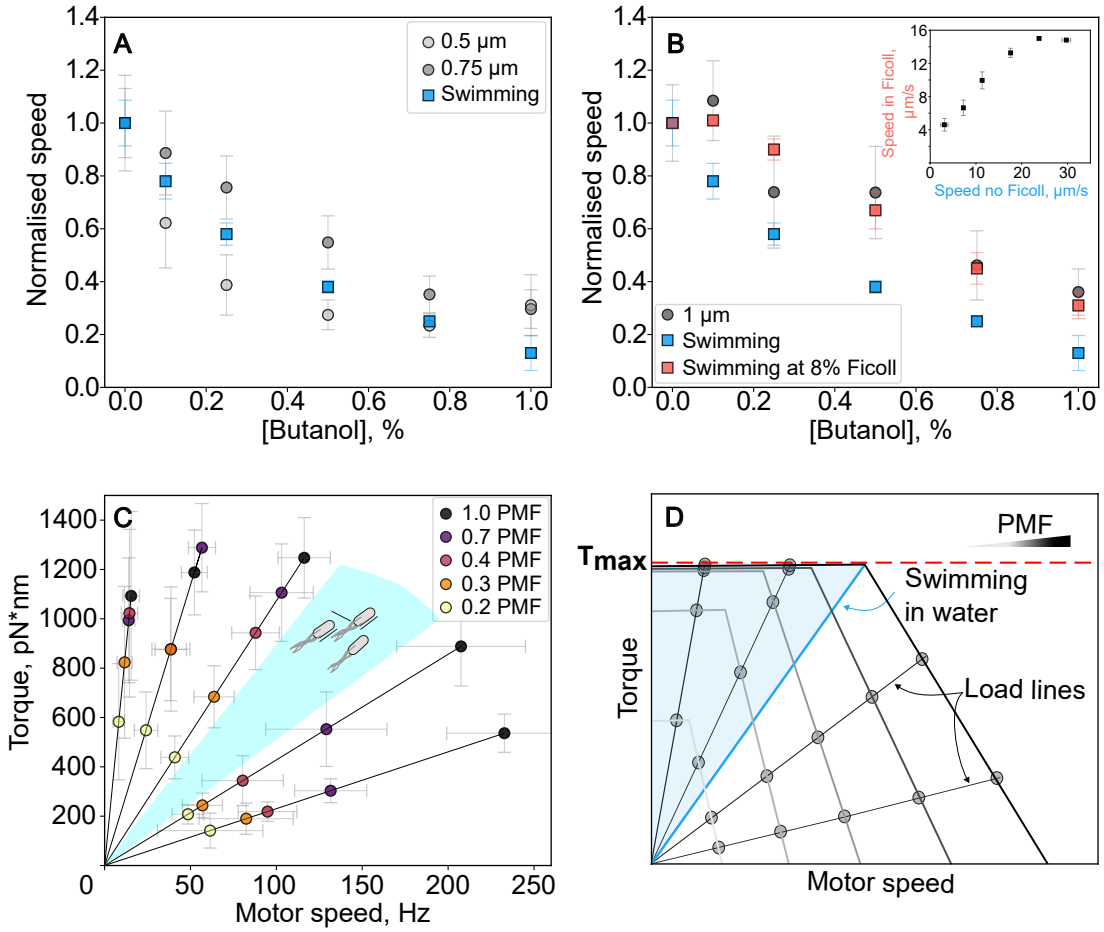

Fig. 3. Free swimming cells produce near-saturation torque. A. The swimming speed response to increasing butanol concentrations is equivalent to the response of BFM under the viscous load imposed by a $\sim 0.6\,\mu\mathrm{m}$ in diameter bead. **B.** Addition of 8% Ficoll increases viscosity 3.5-fold, bringing the load on the motor to that imposed by a $1\,\mu\mathrm{m}$ bead. (***Inset***) Swimming speeds of cells swimming with and without Ficoll are not linearly proportional at high PMF. **C.** Torque-speed curves of the BFM at different different PMFs. Black lines represent load lines for beads of different sizes. Cyan shaded region is the torque-speed space occupied by bacteria swimming freely in an aqueous environment with a viscosity similar to that of water. **D.** A revised cartoon of the idealised torque-speed curves, each depicting BFM torque-speed characteristics at different PMF values (given by the grey colour scale in the top right corner). Straight lines represent load lines. The load line that corresponds to swimming in water shows the lower boundary of the swimming regime, and the light blue shaded region shows the torque-speed space available to *E. coli* when swimming at higher viscosities.

of the load on the motor [22, 27].

The discrepancy could be explained with strain-to-strain differences, where some K12 strains would simply achieve higher absolute PMF values, and thus shift the saturation regime. For example, we used the MG1655 strain, whereas previous work used the RP437 derivative, KAF95 [23, 27, 47, 48]. When grown in the same conditions, these strains have been reported to swim at somewhat different speeds [44]. Therefore, we used the KAF95 strain and compared the motor speeds under the loads imposed by $0.5\,\mu\mathrm{m}$ and $1.5\,\mu\mathrm{m}$ beads, with and without glucose. We found the same saturation at high load as for our strain, SI Fig. 6, eliminating strain-to-strain differences as a possible explanation for the discrepancy.

In Gabel and Berg's experiment, the rotation of two motors was observed in individual KAF95 cells that were genetically modified to rotate only counterclockwise [27]. One motor was anchored to the surface via the filament, in a so-called tethered cell configuration, driving the rotation of the entire cell body, a very high viscous load. The other motor was rotating under a significantly lighter viscous load imposed by a $0.4\,\mu\mathrm{m}$ bead. The cell was chemically treated to collapse the PMF and the rotation of both the cell body and the bead was detected, showing proportionality across the range of PMFs tested. The slow rotation of the cell body was subsequently scaled to the PMF values obtained from a previous experiment [22]. A possible explanation for the discrepancy between this and our observations is that the slow body rotation was not driven by an active motor tethered to the slide, but was rather a passive counter-rotation balancing the torque generated by the second bead-attached motor. In this configuration, the cell would be tethered either by a broken motor or by a hydrophobic patch allowing the cell to pivot passively even in the absence of a flagellum [49]. The observed speeds and the ratio of cell-to-bead rotational friction coefficients are consistent with this explanation (see *Supplementary Material* for exact estimates), as are our own results from a similar experiment with two independently rotating beads attached to the same cell in Fig. 1D.

In Fung and Berg's experiment, a cephalexin-treated filamen-

tous cell was introduced into a microelectrode, and the rotation of the motor located on the portion of the cell outside of the electrode was detected. The motor was operating under a high viscous load imposed by a non-filamentous cell attached to the motor, and the membrane voltage in a range of 0 to -150 mV was applied with a microelectrode [22]. Here, it was assumed that applying a voltage across the entire cell is equivalent to the membrane potential, i.e. charge separation in the few nanometre layer close to the inner membrane [50]. If that is the case, it is hard to explain why the experiment did not observe similar saturation at maximum torque. However, *E. coli* is a gram-negative bacterium, whose inner membrane is shielded from the external environment by the periplasmic space, the cell wall, and the outer membrane. The torque-generating units of the BFM are embedded in the inner membrane and use the electrochemical gradient of protons across the inner membrane only. The conductivity of the inner and outer membranes of *E. coli*, estimated with electrorotation, are 0.5-5 and 5-25 µS/cm, respectively [51]. Thus, it is possible that up to 50% of the potential applied by the microelectrode dropped onto the outer membrane and the maximum voltage on the inner membrane experienced by the motor was lower (in absolute values) than reported; rather than -150 mV it was anywhere between -75 and -150 mV. This estimate includes only the outer membrane and does not consider cell wall and the periplasmic space that could lower the maximum voltage value even more. At the highest load we measured ($1.5\,\mu\mathrm{m}$ beads), torque saturation occurred at $\sim 45\%$ of the maximum PMF, Fig. 2C. If we assume the maximum PMF to be -200 mV[32, 33], the linear range for this load would be 0 to -90 mV, which could indeed be the range tested by Fung and Berg.

Indications of saturation in the PMF-speed proportionality exist in other previous works. Inoue *et al.* found the torque of the chimeric Na^+-driven motor to change significantly with temperature at low load (0.35 µm beads), whereas under high load (1 µm beads) the motor torque was constant at $2000\,\mathrm{pN\,nm}$ irrespective of temperature [52]. Gupta *et al.* reported changes in the swimming speed of *E. coli* with addition of an ionophore, indole, that could not be reproduced in a single motor experiment with 2 µm latex beads [53]. Although alternative explanations were proposed in both studies, the results are also consistent with our finding that the BFM at high loads reaches its saturating torque. In fact, the PMF-speed relationship in Gupta *et al.* [53] obeys the same saturation law observed for high-load beads in Fig. 2B, see SI Fig. 7. Furthermore, Shioi *et al.* [54] and Khan *et al.* [55, 56] reported that the relation between swimming speed and PMF for *Bacillus subtilis* and *Streptococcus* exhibit a threshold at low PMF and a saturation at high PMF. Additionally, Sowa *et al.* reported different relative speed changes for chimeric Na^+-driven motors under low and high loads, with $0.6\,\mu\mathrm{m}$ and $1.08\,\mu\mathrm{m}$ beads respectively yielding 5-fold and 2-fold speed increases for the same change in sodium motive force [57]. This leads us to suggest that the chimeric sodium motor experiences a similar kind of torque-IMF nonlinearity.

Discussion

The bacterial flagellar motor is a sophisticated molecular machine whose structure and operational principles have been extensively studied [6]. However, discovery of new features of the motor forces us to revisit questions long believed to be answered. Here, we addressed the well-known PMF-speed proportionality and found that in *E. coli* it is limited by the maximum motor torque, and that this limit is reached within physiological values of the PMF. Although the existence of such maximum torque is not surprising, the fact that it is reached at physiological PMF was unexpected. Moreover, torque saturation at high loads occurs already at 45% of maximum PMF, Fig. 2C. Consequently, in Fig. 3D we modified previously reported idealised torque-speed curves [25, 27] to include our findings.

Our results enabled us to estimate the viscous load experienced by the motors of swimming cells, the lowest being the equivalent of a $0.6\,\mu\mathrm{m}$ bead in the aqueous medium, see Fig. 3 and *Supplementary Material* for details. Predicting the flagella drag and, thus, motor load using theory is difficult because load sharing between motors and dissipation by filament-body and filament-filament interactions must be taken into account [37, 58]. Our butanol protocols offer a way to measure this load directly and should thus be of interest to the microbial swimming community.

Our results set new limitations on the use of the BFM as a single cell voltmeter to measure PMF [34, 53, 59, 60]. To use the PMF-speed proportionality, it is necessary to confirm that the motor operates below its limiting torque, the lower boundary of which we estimate as $\sim 1250\,\mathrm{pN\,nm}$. As an additional test, we suggest the use of butanol or another ionophore (note that the commonly used protonophore Carbonyl Cyanide m-Chlorophenylhydrazone (CCCP) should be used with care in *E. coli* as it is a substrate for efflux pumps [61]) to probe the sensitivity of motor speed to PMF variations at a given load and in a given condition. This consideration is especially relevant for the use of tethered cells as PMF probes. Their load is typically high but depends on the size of the cell and the geometry of attachment, which can lead to inconsistent results if the saturated regime is reached at different PMFs for different cells. With these limitations in mind, we remain convinced that the BFM in its linear PMF-speed regime is the best PMF sensor currently available [50].

Here, we work with relative rather than absolute PMF variations, assuming that PMF in MM9+20 mM glucose is close to the maximum physiological value. While absolute PMF measurements in live Gram-negative bacteria such as *E. coli* remain challenging [50], some estimates of the PMF achieved by respiring *E. coli* are available: a theoretical study predicted a range of -170 mV to -229 mV from the free energies of NADH oxidation and ATP hydrolysis [62], and values of -230 mV and -160 mV were estimated from proton and potassium fluxes in *E. coli* spheroplasts [32], and by radioactive probing [33], respectively. Using those estimates, relative PMF variations recorded by BFM speed measurements can be converted to absolute PMF values.

Our estimates of maximum torque, $1250\text{-}1800\,\mathrm{pN\,nm}$, are

within the range of previously published values for a wild type *E. coli* motor: Reid *et al.* estimated the maximum torque to be $1260 \pm 190\,\mathrm{pN\,nm}$ [12], Ryu *et. al* measured torque up to $\sim 1300\,\mathrm{pN\,nm}$ [24], and Berry *et al.* reported a stall torque of $4500\,\mathrm{pN\,nm}$ [63], which was later corrected to $\sim 2000\,\mathrm{pN\,nm}$ [6, 36]. Estimates of the torque produced by a single stator unit: 146 [12], 250 [64], or $320\,\mathrm{pN\,nm}$ [24], with up to 11-12 stator units per motor [12], are also in line with our result. Here, for better comparison with previous torque estimates, we applied the equation most commonly used for torque calculation in the bead assay (see *Materials and Methods*) [15, 24, 26, 52], and did not include hydrodynamic surface effects between the cell body and the rotating bead [64]. We discuss in *Supplementary Material* the possible origins of the relatively large variability in our assay, but stress that our two main conclusions are robust to those variations: the saturation of the PMF-speed relationship at high loads was observed across all experiments, and the value of the swimming load ($0.6\,\mu\mathrm{m}$ bead equivalent) obtained from butanol experiments was independent of the initial motor speed (see *Supplementary Material*).

Although our work shows that the PMF-speed saturation occurs at physiological PMF under medium-to-high load, it does not address why evolution sets the limiting torque to its current value. One possible explanation is that it is sufficiently high to never hamper *E. coli*'s chemotactic efficiency in natural environments. Indeed, while *E. coli*'s primary habitat, the gastrointestinal tract of warm-blooded animals, is presumably much more viscous than water, it is also mostly anaerobic, which means that *E. coli*'s PMF in this environment is likely significantly lower than in our aerobic experiments. At the same time, *E. coli* cells swimming outside a host presumably experience low viscous loads and are unlikely to be as fully energised as in our glucose experiments. In both cases, it is possible that a higher limiting torque would not significantly benefit the cells since a PMF high enough for saturation is never reached. Alternatively, maintaining a constant, PMF-independent speed in the saturated regime might also confer some advantages by preventing cells from accumulating in low-PMF regions in the absence of an attractant/repellent gradient.

The nonlinear nature of the PMF-speed dependency challenges BFM models that assume tight coupling between the ion flux and the motor rotation [7, 25, 65], given that the PMF-speed linearity is a necessary condition for such models. Therefore, our finding sets a new critical constraint to BFM mechanistic modelling. Lastly, and in addition to revising the long-held view that the BFM speed is universally proportional to PMF in *E. coli*, our study raises new questions about the motility strategies employed by *E. coli* in natural environments.

Materials and Methods

Bacteria culturing and media. For BFM speed measurements we used EK01 strain, a derivative of MG1655 with the flagellin encoding *fliC* gene replaced by *fliC*^{sticky} [66]. The mutation makes flagella hydrophobic and allows polystyrene beads to stick to them by electrostatic interaction. The KAF95 strain was also used for comparison with previous work [27]. This RP437 derivative strain bears a *FliC* and *cheY* deletion, the latter making its motor rotate exclusively counterclockwise, as well as an ampicillin-resistant plasmid encoding the *fliC*^{sticky} mutation.

The bacteria were grown in Lysogeny Broth (LB: 10 g tryptone, 5 g yeast extract, 10 g NaCl per 1 L). The overnight culture (OD=5.5) frozen and stored at -80°C in the presence of 20% glycerol was thawed and diluted in fresh LB to $\mathrm{OD} \approx 0.003$ (1:1000 dilution of the overnight culture) and grown at 37°C with shaking (220 rpm) to $\mathrm{OD} = 2.0$. After harvesting, cells were "sheared" by multiple passing through a narrow gauge needle [67], and washed 3 times by centrifugation (8000 g, 2 min) into MM9 (aqueous solution of 50 mM Na_2HPO_4, 25 mM NaH_2PO_4, 8.5 mM NaCl and 18.7 mM NH_4Cl with added 0.1 mM $CaCl_2$, 1 mM KCl, 2 mM $MgSO_4$, pH=7), with or without glucose. For butanol experiments, MM9+20 mM glucose was supplemented with 1-butanol (molecular biology grade, Sigma-Aldrich) to desired concentration.

To measure the speed of multiple motors on elongated cells, EK01 were grown in the presence of cephalexin. Cells were grown to $\mathrm{OD} \approx 1$, at which point $50\,\mu\mathrm{L}$ of a $10\,\mathrm{mg\,mL^{-1}}$ cephalexin aqueous stock solution was added to $10\,\mathrm{mL}$ of culture ($50\,\mu\mathrm{g\,mL^{-1}}$ final cephalexin concentration). Cells were grown for an additional 45-60 min to $\mathrm{OD} \approx 2$ before being harvested and prepared for the bead assay.

Swimming speed measurements were conducted with strain AD80, a smooth-swimming MG1655 mutant constructed by deleting the *cheY* gene [44]. Bacteria were grown in LB to $\mathrm{OD} = 2$ at $37\,^{\circ}\mathrm{C}$ with shaking (220 rpm), harvested and washed by filtration [44] in MM9+20 mM glucose. The concentrated suspension obtained was diluted with MM9+20 mM glucose and stored on ice until differential dynamic microscopy measurement.

BFM speed recording with bead assay. For BFM speed recording, we used the bead assay [19] in combination with back-focal-plane interferometry (BFP) [3, 68, 69] or a high-speed camera (iDS uEye CP and Teledyne Photometrics Prime 95B) for all bead sizes. BFP interferometry has a higher temporal resolution but a much lower throughput than the camera. Both methods were used to ensure they returned identical results, but most of the data were collected with the cameras, and the data sets were later merged into a single speed distribution for a given condition (see SI Fig. 1 and 2) .

For the bead assay, cells were immobilised on glass tunnel slides, and polystyrene beads of given sizes were attached to their truncated flagella [70]. The medium in the tunnel was refreshed every 5-10 min by flushing $100\,\mu\mathrm{L}$ of fresh medium to ensure that glucose and oxygen were not depleted during recording. For BFP interferometry, time course of the bead rotation was recorded with the position-sensitive detector (PSD Model 2931, New Focus, USA) at 10 kHz sampling rate for 10 s per motor. For high-speed camera, the frame rate was 460 fps for slow motors and 1200 fps for all motors (slow

motors were recorded with both settings) with 2-35 motors per field of view being recorded simultaneously for 10 s. For experiments with cephalexin-treated cells, all media were supplemented with $50\,\mu\mathrm{g\,mL^{-1}}$ cephalexin. The beads were trajectories recorded using the high-speed camera at 1200 fps.

Differential dynamic microscopy. For swimming speed measurements in the absence of Ficoll, washed cells were stored at $\mathrm{OD} = 1$ on ice. For each butanol concentration, $150\,\mu\mathrm{L}$ of this suspension was diluted to $\mathrm{OD} = 0.3$ with $350\,\mu\mathrm{L}$ of MM9+20 mM glucose supplemented with an appropriate butanol concentration. $200\,\mu\mathrm{L}$ of this suspension was used immediately to fill a rectangle glass capillary (VitroCom, inner diameters $0.4\,\mathrm{mm} \times 8\,\mathrm{mm}$). The capillary was sealed with petroleum jelly (Vaseline) to prevent evaporation, and bacteria were imaged with a phase contrast objective (Plan Fluor 10×/0.3), approximately $150\,\mu\mathrm{m}$ above the bottom of the capillaries. 40-s long movies were recorded at 100 fps using an Orca Flash 4.0 camera (Hamamatsu).
For experiments with Ficoll 400 (Sigma Aldrich), washed cells were stored at $\mathrm{OD} = 3$ on ice. $50\,\mu\mathrm{L}$ of this suspension was diluted to $\mathrm{OD} = 0.3$ with $450\,\mu\mathrm{L}$ MM9+20 mM glucose supplemented with an appropriate butanol concentration and 9 wt% Ficoll (resulting in 8.1 wt% final Ficoll concentration). Capillaries were prepared and imaged as described above.
For viscosity measurements (see SI), $0.5\,\mu\mathrm{m}$ and $1\,\mu\mathrm{m}$ polystyrene beads (2.5 wt% initial concentration) were diluted 10x in either deionized water or $\mathrm{MM9} + 20\,\mathrm{mM}$ glucose +9 wt% Ficoll (8 wt% final Ficoll concentration), and the resulting suspensions were imaged using the same conditions as for the swimming speed measurements (see also *Supplementary Material*). Viscosities were calculated using the Stokes-Einstein relation from the measured diffusivities.

Data analysis.

Single motor's speed calculation. BFP interferometry output was given in x-y coordinates calculated from the PSD photocurrents as described in [34]. For high-speed camera recordings, ROI was manually selected in FIJI/ImageJ, Otsu threshold was applied to each ROI, and the coordinates of the center of mass of the binary image were calculated for each frame giving the x-y time series of the bead rotation. Alternatively, bead trajectories were recorded via direct tracking in MATLAB R2022a, using a code adapted from ref. [71]. Both methods returned identical results when applied to the same data sets.
The rotational frequencies were then extracted by using a fast Fourier transform (FFT) on the x-y series. A flat-top window discrete Fourier transform (window size of 16384 data points for BFP interferometry data and 1024 for high-speed camera data, 0.1 s sliding window step) was applied to the bead coordinates to obtain a time series of motor speeds. The mean speed was calculated for each motor and the mean and standard deviation of the population were calculated for each condition (speed distributions in SI Fig. 1 and 2).

Swimming speed and viscosity measurements. DDM movies were analysed using previously described methods [45, 43]. The average speed of the suspension was obtained for each movie by assuming that the speed distribution of motile *E. coli* cells takes Schulz form:

$$P(v) = \frac{v^Z}{Z!}\left(\frac{Z+1}{\bar{v}}\right)^{Z+1} e^{-\frac{v}{\bar{v}}(Z+1)}, \qquad \textbf{(1)}$$

where $\bar{v}$ is the mean of the speed distribution and the variance σ_v^2 of $P(v)$ is related to Z via $\sigma_v^2 = \frac{\bar{v}^2}{Z+1}$.
For the viscosity measurements, the diffusivity D of diffusing spheres (see Differential dynamic microscopy subsection) was obtained by using the following intermediate scattering function in DDM analysis [72]:

$$f(q,\tau) = e^{-Dq^2\tau}, \qquad \textbf{(2)}$$

where q is the wave vector and τ the time.

Torque calculations. The torque was calculated as before [15, 24, 26, 52]:

$$T = f_\mathrm{r}\omega = (f_\mathrm{b} + f_\mathrm{f})\omega = 2\pi(f_\mathrm{b} + f_\mathrm{f})s, \qquad \textbf{(3)}$$

where T is torque, f_r is the rotational frictional drag coefficient and ω is the angular velocity of the BFM, i.e. its speed (s) obtained by FFT in Hz and multiplied by 2π. f_r is the sum of the drag coefficients of the flagellar filament stub (f_f) and the attached bead (f_b). The filament stub contribution was estimated as $f_\mathrm{f} \approx 0.1\,\mathrm{pN\,nm\,Hz^{-1}}$ (mean of values reported in [52] and [73] divided by 2π). f_b was calculated as:

$$f_b = 8\pi\eta {r_\mathrm{b}}^3 + 6\pi\eta r_\mathrm{b} {r_\mathrm{r}}^2, \qquad \textbf{(4)}$$

where r_b is the radius of the bead, r_r is the eccentricity of the bead's rotation and η is the viscosity. η was set to $1\,\mathrm{mPa\,s}$ and r_r to 200 nm (values measured from the videos were 100-320 nm).
Note that multiple studies used frequency instead of angular velocity in Eq. 3, thus, having to multiply the rotational frictional drag coefficient by 2π.

ACKNOWLEDGEMENTS
We would like to thank all members of the Pilizota, Poon, and Lo labs, especially Chao-Kai Tseng, as well as Calin Guet for their support and useful discussions. TP, EK, and CJL were supported by the Human Frontier Science Program grant (RGP0041/2015), EK was supported by the EMBO Long-Term Fellowship ALTF 44-2021 and the Scottish Universities Physics Alliance (SUPA) Short-Term Visit Funding Scheme to CJL's lab. TP and LLN were supported by the Leverhulme Trust grant RPG-2019-187 and the EPSRC established career fellowship EP/V03264X/1. CJL was supported by NSTC Taiwan (NSTC-109-2628-M-008-01-MY4).

References

1. HC Berg, RA Anderson, Bacteria swim by rotating their flagellar filaments. *Nature* **245**, 380–382 (1973).

2. J Adler, Chemotaxis in bacteria. *Annu. Rev. Biochem.* **44**, 341–356 (1975).

3. J Rosko, V Martinez, W Poon, T Pilizota, Osmotaxis in *Escherichia coli* through changes in motor speed. *Proc. Natl. Acad. Sci. U. S. A.* **114**, E7969–E7976 (2017).

4. A Paulick, et al., Mechanism of bidirectional thermotaxis in *Escherichia coli*. *eLife* **6**, e26607 (2017).

5. BL Taylor, How do bacteria find the optimal concentration of oxygen? *Trends Biochem. Sci.* **8**, 438–441 (1983).

6. Y Sowa, RM Berry, Bacterial flagellar motor. *Q. Rev. Biophys.* **41**, 103–132 (2008).

7. JA Nirody, YR Sun, CJ Lo, The biophysicist's guide to the bacterial flagellar motor. *Adv. Phys. X* **2**, 324–343 (2017).

8. AG Stewart, EM Laming, M Sobti, D Stock, Rotary ATPases—dynamic molecular machines. *Curr. Opin. Struct. Biol.* **25**, 40–48 (2014).

9. H Guo, T Suzuki, JL Rubinstein, Structure of a bacterial ATP synthase. *eLife* **8**, e43128 (2019).

10. H Hu, et al., Structure and mechanism of zorya antiphage defense system. *bioRxiv* (2023).

11. S Kojima, DF Blair, Solubilization and purification of the MotA/MotB complex of *Escherichia coli*. *Biochemistry* **43**, 26–34 (2004).

12. SW Reid, et al., The maximum number of torque-generating units in the flagellar motor of *Escherichia coli* is at least 11. *Proc. Natl. Acad. Sci. U. S. A.* **103**, 8066–8071 (2006).

13. PP Lele, BG Hosu, HC Berg, Dynamics of mechanosensing in the bacterial flagellar motor. *Proc. Natl. Acad. Sci. U. S. A.* **110**, 11839–11844 (2013).

14. MJ Tipping, NJ Delalez, R Lim, RM Berry, JP Armitage, Load-dependent assembly of the bacterial flagellar motor. *mBio* **4** (2013).

15. AL Nord, et al., Catch bond drives stator mechanosensitivity in the bacterial flagellar motor. *Proc. Natl. Acad. Sci. U. S. A.* **114**, 201716002 (2017).

16. SH Larsen, J Adler, JJ Gargus, RW Hogg, Chemomechanical coupling without ATP: the source of energy for motility and chemotaxis in bacteria. *Proc. Natl. Acad. Sci. U. S. A.* **71**, 1239–1243 (1974).

17. P Mitchell, Coupling of phosphorylation to electron and hydrogen transfer by a chemi-osmotic type of mechanism. *Nature* **191**, 144–148 (1961).

18. DG Nicholls, SJ Ferguson, *Bioenergetics 2*. (Academic Press), p. 272 (1992).

19. E Krasnopeeva, UE Barboza-Perez, J Rosko, T Pilizota, CJ Lo, Bacterial flagellar motor as a multimodal biosensor. *Methods* **193**, 5–15 (2021).

20. A Biquet-Bisquert, G Labesse, F Pedaci, AL Nord, The dynamic ion motive frce powering the bacterial flagellar motor. *Front. Microbiol.* **12** (2021).

21. MC Leake, et al., Stoichiometry and turnover in single, functioning membrane protein complexes. *Nature* **443**, 355–358 (2006).

22. DC Fung, HC Berg, Powering the flagellar motor of *Escherichia coli* with an external voltage source. *Nature* **375**, 809–812 (1995).

23. X Chen, HC Berg, Torque-speed relationship of the flagellar rotary motor of *Escherichia coli*. *Biophys. J.* **78**, 1036–1041 (2000).

24. WS Ryu, RM Berry, HC Berg, Torque-generating units of the flagellar motor of *Escherichia coli* have a high duty ratio. *Nature* **403**, 444–447 (2000).

25. J Xing, F Bai, R Berry, G Oster, Torque–speed relationship of the bacterial flagellar motor. *Proc. Natl. Acad. Sci. U. S. A.* **103**, 1260–1265 (2006).

26. C Lo, Y Sowa, T Pilizota, RM Berry, Mechanism and kinetics of a sodium-driven bacterial flagellar motor. *Proc. Natl. Acad. Sci. U. S. A.* **110**, E2544–E2551 (2013).

27. CV Gabel, HC Berg, The speed of the flagellar rotary motor of *Escherichia coli* varies linearly with protonmotive force. *Proc. Natl. Acad. Sci. U. S. A.* **100**, 8748–8751 (2003).

28. N Hirota, M Kitada, Y Imae, Flagellar motors of alkalophilic *Bacillus* are powered by an electrochemical potential gradient of Na^+. *FEBS Lett.* **132**, 278–280 (1981).

29. N Hirota, Y Imae, Na^+-driven flagellar motors of an alkalophilic *Bacillus* strain YN-1. *J. Biol. Chem.* **258**, 10577–10581 (1983).

30. B Chernyak, P Dibrov, A Glagolev, M Sherman, V Skulachev, A novel type of energetics in a marine alkalitolerant bacterium: $\Delta\bar{\mu}_{\mathrm{Na}}$ -driven motility and sodium cycle. *FEBS Lett.* **164**, 38–42 (1983).

31. CJ Lo, MC Leake, T Pilizota, RM Berry, Nonequivalence of membrane voltage and ion-gradient as driving forces for the bacterial flagellar motor at low load. *Biophys. J.* **93**, 294–302 (2007).

32. SH Collins, WA Hamilton, Magnitude of the protonmotive force in respiring *Staphylococcus aureus* and *Escherichia coli*. *J. Bacteriol.* **126**, 1224–1231 (1976).

33. QH Tran, G Unden, Changes in the proton potential and the cellular energetics of *Escherichia coli* during growth by aerobic and anaerobic respiration or by fermentation. *Eur. J. Biochem.* **251**, 538–543 (1998).

34. E Krasnopeeva, CJ Lo, T Pilizota, Single-cell bacterial electrophysiology reveals mechanisms of stress-induced damage. *Biophys. J.* **116**, 2390–2399 (2019).

35. CC Chung, IF Cheng, WH Yang, HC Chang, Antibiotic susceptibility test based on the dielectrophoretic behavior of elongated *Escherichia coli* with cephalexin treatment. *Biomicrofluidics* **5**, 021102 (2011).

36. KK Mandadapu, JA Nirody, RM Berry, G Oster, Mechanics of torque generation in the bacterial flagellar motor. *Proc. Natl. Acad. Sci. U. S. A.* **112**, E4381–E4389 (2015).

37. NC Darnton, L Turner, S Rojevsky, HC Berg, On Torque and Tumbling in Swimming *Escherichia coli*. *J. Bacteriol.* **189**, 1756–1764 (2007).

38. D Das, E Lauga, Computing the motor torque of *Escherichia coli*. *Soft matter* **14**, 5955–5967 (2018).

39. G Vizsnyiczai, et al., A transition to stable one-dimensional swimming enhances *E. coli* motility through narrow channels. *Nat. Commun.* **11**, 2340 (2020).

40. VA Martinez, et al., Flagellated bacterial motility in polymer solutions. *Proc. Natl. Acad. Sci. U. S. A.* **111**, 17771–17776 (2014).

41. Y Niu, R Zhang, J Yuan, Flagellar motors of swimming bacteria contain an incomplete set of stator units to ensure robust motility. *Sci. Adv.* **9**, eadi6724 (2023).

42. I Lisevich, R Colin, HY Yang, B Ni, V Sourjik, Physics and physiology determine strategies of bacterial investment in flagellar motility. *bioRxiv*, 2024–03 (2024).

43. LG Wilson, et al., Differential dynamic microscopy of bacterial motility. *Phys. Rev. Lett.* **106**, 018101 (2011).

44. J Schwarz-Linek, et al., *Escherichia coli* as a model active colloid: A practical introduction. *Colloids Surf. B Biointerfaces* **137**, 2–16 (2016).

45. VA Martinez, et al., Differential dynamic microscopy: A high-throughput method for characterizing the motility of microorganisms. *Biophys. J.* **103**, 1637–1647 (2012).

46. Z Qu, FZ Temel, R Henderikx, KS Breuer, Changes in the flagellar bundling time account for variations in swimming behavior of flagellated bacteria in viscous media. *Proc. Natl. Acad. Sci. U. S. A.* **115**, 1707–1712 (2018).

47. JS Parkinson, SE Houts, Isolation and behavior of *Escherichia coli* deletion mutants lacking chemotaxis functions. *J. Bacteriol.* **151**, 106–113 (1982).

48. HC Berg, L Turner, Torque generated by the flagellar motor of *Escherichia coli*. *Biophys. J.* **65**, 2201–16 (1993).

49. T Vissers, et al., Bacteria as living patchy colloids: Phenotypic heterogeneity in surface adhesion. *Sci. Adv.* **4**, eaao1170 (2018).

50. WC Lo, E Krasnopeeva, T Pilizota, Bacterial Electrophysiology. *Annu. Rev. Biophys.* **53**, 487–510 (2024).

51. R Hölzel, Non-invasive determination of bacterial single cell properties by electrorotation. *Biochim. et Biophys. Acta (BBA) - Mol. Cell Res.* **1450**, 53–60 (1999).

52. Y Inoue, et al., Temperature dependences of torque generation and membrane voltage in the bacterial flagellar motor. *Biophys. J.* **105**, 2801–2810 (2013).

53. R Gupta, et al., Indole modulates cooperative protein–protein interactions in the flagellar motor. *PNAS Nexus* **1**, pgac035 (2022).

54. JI Shioi, S Matsuura, Y Imae, Quantitative measurements of proton motive force and motility in *Bacillus subtilis*. *J. Bacteriol.* **144**, 891–897 (1980).

55. S Khan, RM Macnab, The steady-state counterclockwise/clockwise ratio of bacterial flagellar motors is regulated by protonmotive force. *J. Mol. Biol.* **138**, 563–597 (1980).

56. S Khan, M Dapice, I Humayun, Energy transduction in the bacterial flagellar motor. Effects of load and pH. *Biophys. J.* **57**, 779–796 (1990).

57. Y Sowa, H Hotta, M Homma, A Ishijima, Torque-speed relationship of the Na^+-driven flagellar motor of *Vibrio alginolyticus*. *J. Mol. Biol.* **327**, 1043–1051 (2003).

58. S Kamdar, et al., Multiflagellarity leads to the size-independent swimming speed of peritrichous bacteria. *Proc. Natl. Acad. Sci. U. S. A.* **120**, e2310952120 (2023).

59. JM Kralj, DR Hochbaum, AD Douglass, AE Cohen, Electrical spiking in *Escherichia coli* probed with a fluorescent voltage-indicating protein. *Science* **333**, 345–348 (2011).

60. X Jin, et al., Sensitive bacterial V_m sensors revealed the excitability of bacterial V_m and its role in antibiotic tolerance. *Proc. Natl. Acad. Sci. U. S. A.* **120**, e2208348120 (2023).

61. D Le, E Krasnopeeva, F Sinjab, T Pilizota, M Kim, Active efflux leads to heterogeneous dissipation of proton motive force by protonophores in bacteria. *mBio* **12**, e00676–21 (2021).

62. G Terradot, E Krasnopeeva, PS Swain, T Pilizota, The proton motive force determines *Escherichia coli's* robustness to extracellular pH. *bioRxiv* (2021).

63. RM Berry, HC Berg, Absence of a barrier to backwards rotation of the bacterial flagellar motor demonstrated with optical tweezers. *Proc. Natl. Acad. Sci. U. S. A.* **94**, 14433–14437 (1997).

64. B Wang, G Yue, R Zhang, J Yuan, Direct measurement of the stall torque of the flagellar motor in *Escherichia coli* with magnetic tweezers. *mBio* **13**, e00782–22 (2022).

65. M Meister, S Caplan, H Berg, Dynamics of a tightly coupled mechanism for flagellar rotation. Bacterial motility, chemiosmotic coupling, protonmotive force. *Biophys. J.* **55**, 905–914 (1989).

66. G Kuwajima, Construction of a minimum-size functional flagellin of *Escherichia coli*. *J. Bacteriol.* **170**, 3305–3309 (1988).

67. T Pilizota, J Rosko, E Krasnopeeva, BFM speed recording with back-focal-plane interferometry. *dx.doi.org/10.17504/protocols.io.bch2it8e* (2021).

68. W Denk, WW Webb, Optical measurement of picometer displacements of transparent microscopic objects. *Appl. Opt.* **29**, 2382–2391 (1990).

69. K Svoboda, CF Schmidt, BJ Schnapp, SM Block, Direct observation of kinesin stepping by optical trapping interferometry. *Nature* **365**, 721–727 (1993).

70. UB Perez, E Krasnopeeva, J Rosko, T Pilizota, Tunnel slide preparation for motor speed recordings. *dx.doi.org/10.17504/protocols.io.bcjdiui6* (2021).

71. D Blair, E Dufresne, The Matlab particle tracking code repository (http://site.physics.georgetown.edu/matlab/) (2008).

72. JJ Bradley, VA Martinez, J Arlt, JR Royer, WC Poon, Sizing multimodal suspensions with differential dynamic microscopy. *Soft Matter* **19**, 8179–8192 (2023).

73. CJ Lo, Ph.D. thesis (University of Oxford) (2007).

74. CV Gabel, Ph.D. thesis (Harvard University) (2003).

Supplementary Material

Supplementary Figures and Tables. Figures are given in the order mentioned in the main text, followed by mentions in the *Supplementary Material* text.

Nominal bead diameter, μm	Actual bead diameter, μm
0.35	0.370, CV=4% 0.356±0.014
0.5	0.51, CV=2%
0.75	0.746, CV=3% 0.771±0.025
1	1.06, CV=1% 0.99, CV=3%
1.5	1.54, CV=4% 1.537±0.056

Table 1. Bead diameters used in the experiments.

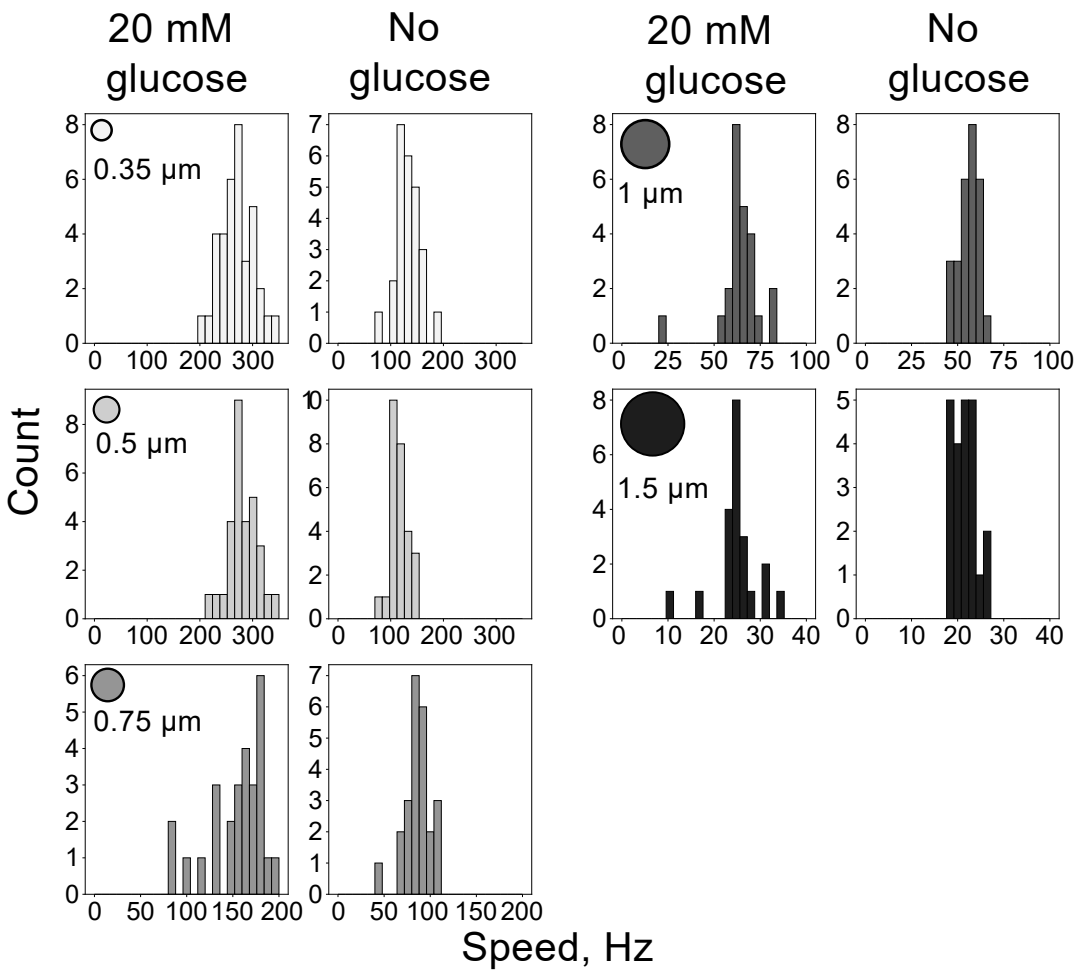

SI Fig. 1. Motor speed distributions, supplementary to Fig. 1A. Histograms of motor speeds for each experiment with and without glucose (25 bins are used for a given range). Bead colour coding is the same as in the main text.

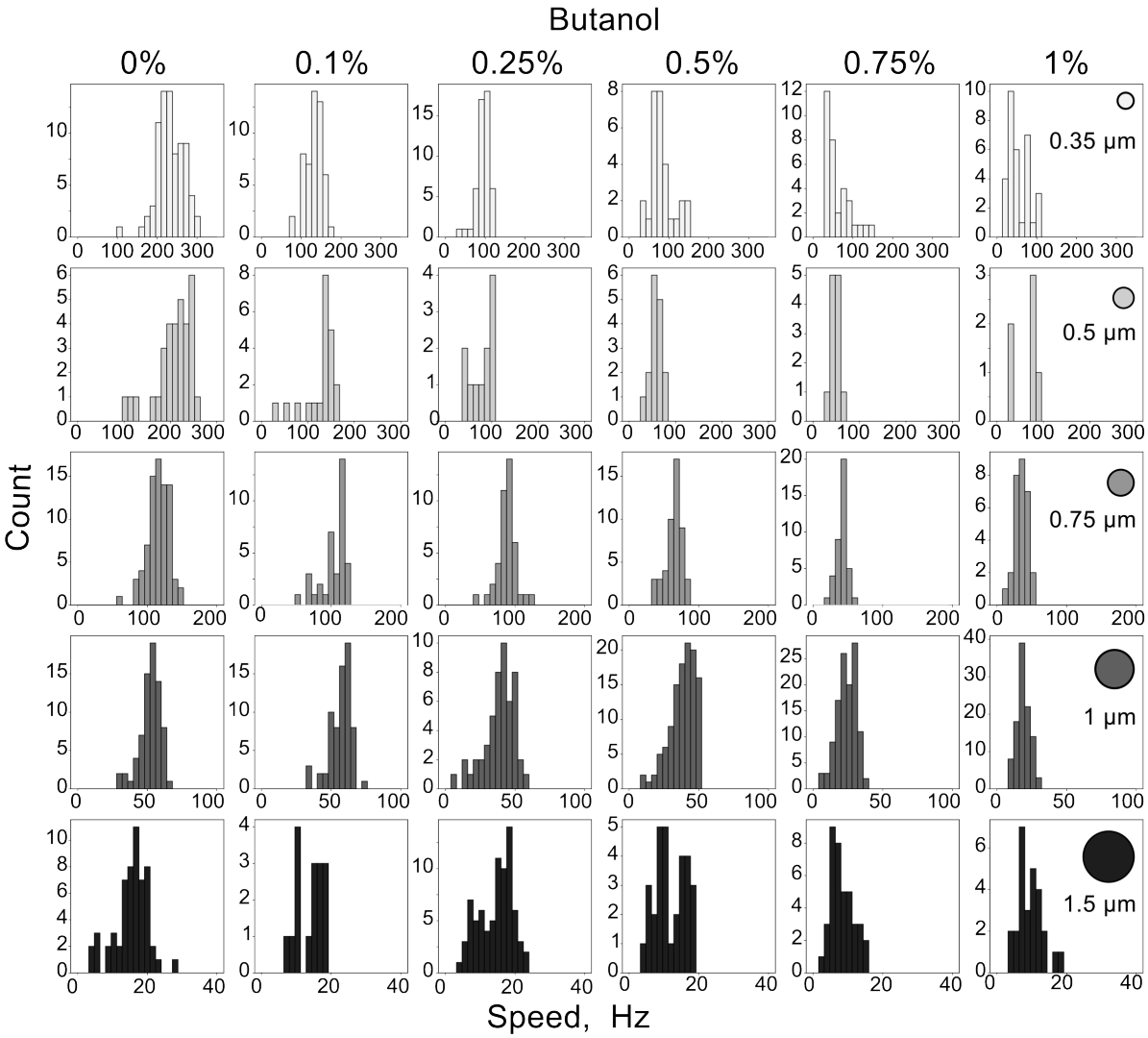

SI Fig. 2. Motor speed distributions, supplementary to Fig. 1C. Histograms of motor speeds for all butanol experiments (25 bins are used for a given range). Bead colour coding is the same as in the main text.

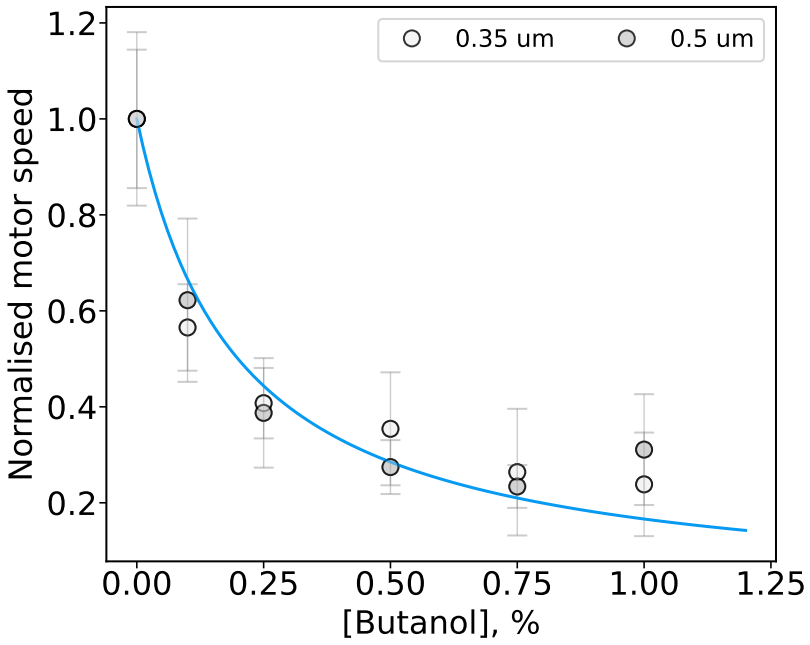

SI Fig. 3. Calibration curve for converting butanol concentration to relative change in the PMF. Speed-butanol curve is fitted with a hyperbola $S = \frac{1}{k*c_{but}+1}$, where c_{but} is butanol concentration in volume/volume percentage, S is a relative motor speed, and $k = 5.01$ is a fitted constant. Since normalised motor speed of the BFM under low viscous load is assumed to be proportional to PMF, the equation for normalised PMF is also $\mathrm{PMF} = \frac{1}{k*c_{but}+1}$. Data points show mean speed at a given butanol concentration normalised to the speed in the absence of butanol, error bars show standard deviation of the mean.

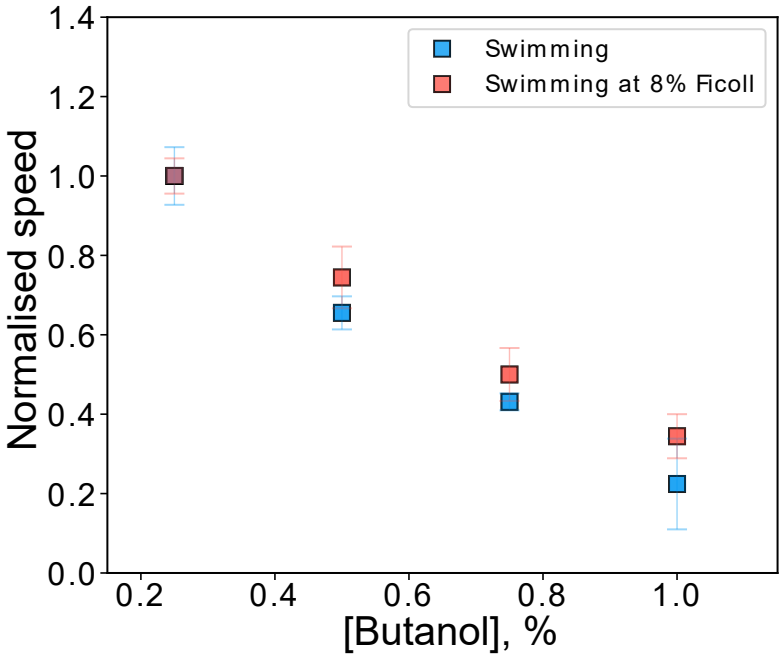

SI Fig. 4. Free swimming speeds with and without Ficoll from Fig. 3B collapse to the same curve for low PMF values. Here, motor speeds are normalised to the speed at 0.25% butanol, corresponding to 44% of maximum PMF. Data points show mean with the standard deviation.

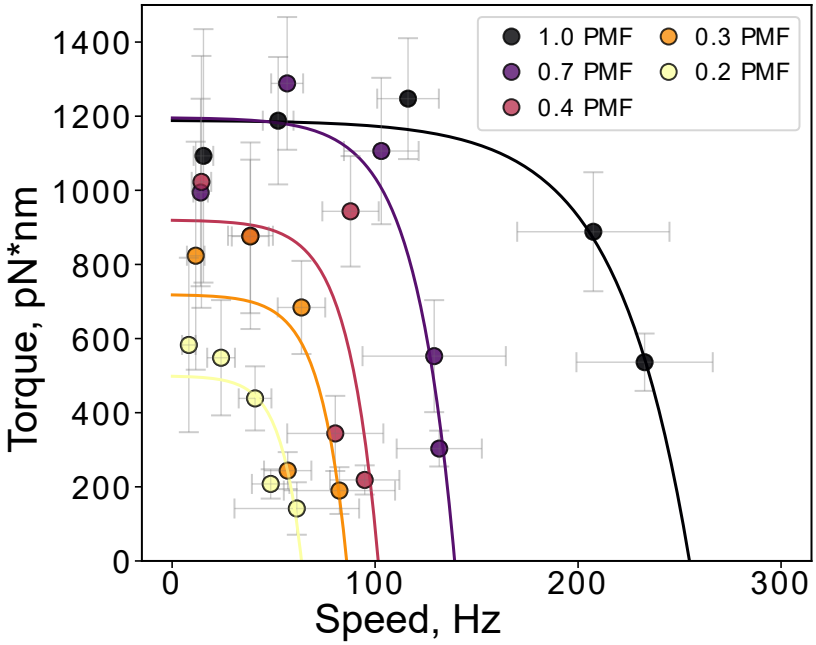

SI Fig. 5. Torque-speed curves for data in Fig. 1C. Motor torque is calculated as described in *Methods* section, and, as before, the PMF is scaled to PMF of a bacterium in MM9+20 mM glucose medium with no butanol added. The fits are exponential decay curves $T = T_{max} - e^{\frac{S}{S_0}}$, where S is a motor speed in Hz, and S_0 is a free fitting parameter. Data points show mean with the standard deviation.

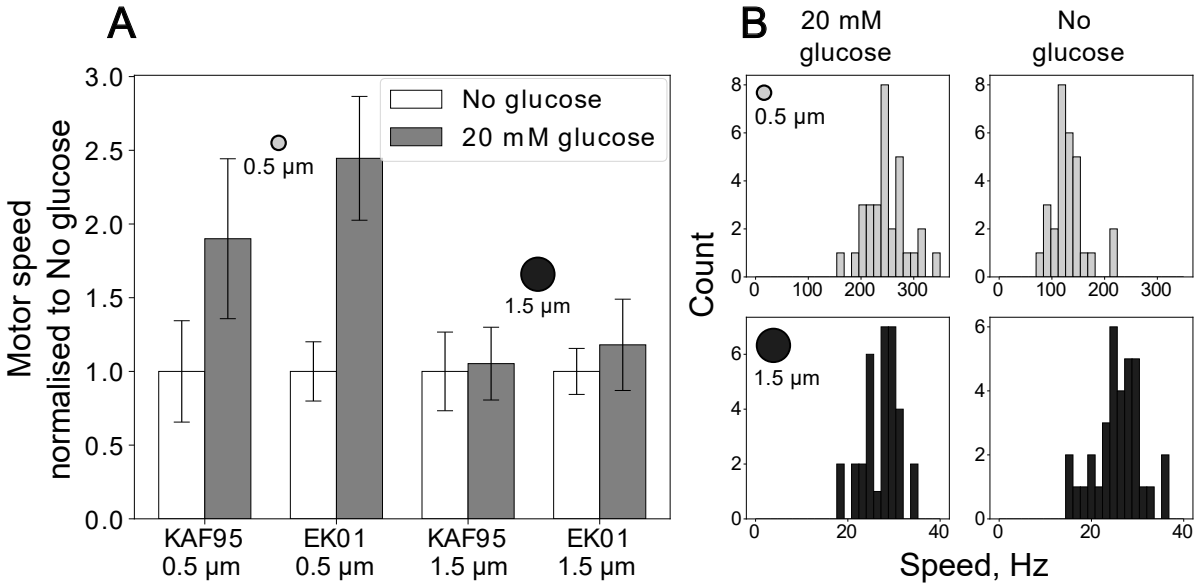

SI Fig. 6. The torque saturation effect is reproducible with KAF95 strain (RP437 derivative). A. Relative speed change for cells with and without glucose is different under 0.5 or 1.5 μm beads load but similar to that of the EK01 strain (MG1655 derivative) used in this work. **B.** Speed histograms for data in A. Histograms are plotted in ranges (0,350) for 0.5 μm and (0,40) for 1.5 μm beads (25 bins are used for each range). Bead colour coding is the same as in the main text. Error bars show standard deviation of the mean.

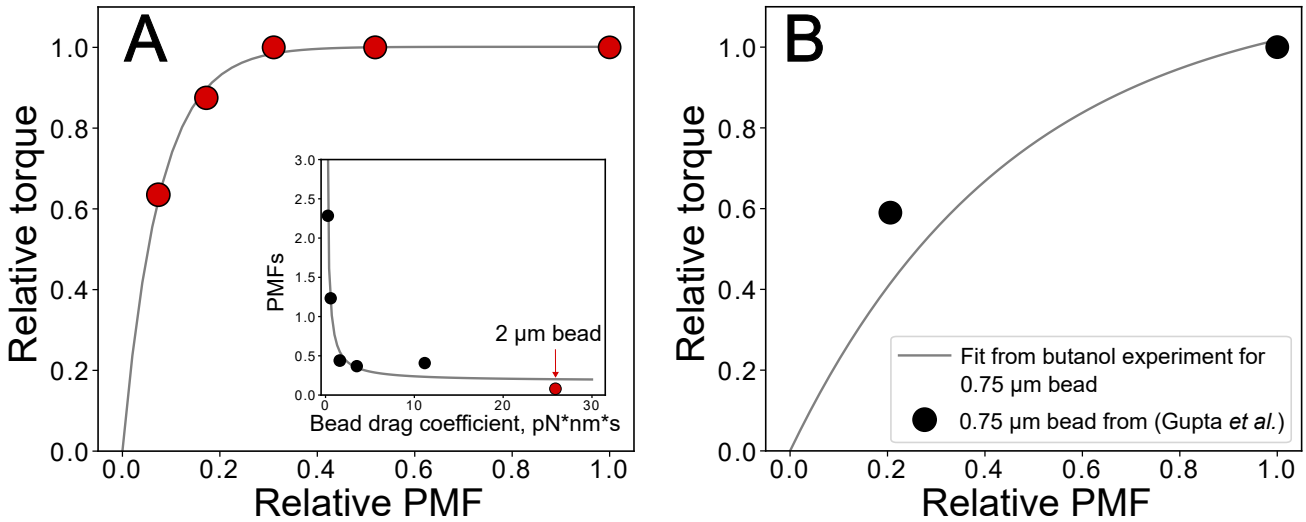

SI Fig. 7. PMF-torque saturation in Gupta *et al.* A. PMF-torque saturation for 2 μm bead from previous work is consistant with this work. The speed data are taken from Gupta *et al.* for cells treated with 0, 0.5, 1, 2, and 5 mM indole [53]. Indole concentrations are converted to PMF similarly to butanol, based on the calibration curve from Krasnopeeva *et al.*: $PMF = \frac{1}{k*c_{ind}+c_0}$, where c_{ind} is indole concentration in mM, and $k = 2.58\ mM^{-1}$ and $c_0 = -0.365$ are fitted constants [34]. The maximum torque, calculated for a 2 μm bead rotating at 10 Hz with 200 nm rotation radius in aqueous environment, is $1630\,\mathrm{pN\,nm}$, and so within the range we estimated for maximum torque $(1250\text{-}1800\,\mathrm{pN\,nm})$. The curve shows the exponential fit as in Fig. 2B: $T = T_{\max}(1 - e^{-\frac{\mathrm{PMF}}{\mathrm{PMF_s}}})$, where T_{max}=$1630\,\mathrm{pN\,nm}$, and $\mathrm{PMF_s} = 0.08$. Torque is normalised to the value at PMF=1, which corresponds to cells in MM9+20 mM glucose with no indole added. (***Inset***) $\mathrm{PMF_s}$ for 2 μm bead is added to the plot from Fig. 2C, and the hyperbolic curve ($y = \frac{a}{b*x+c}$, where $a = 781.7, b = 473.5$, and $c = 15.47$ are free parameters) is fitted to all the data points. **B.** PMF-torque saturation for 0.75 μm bead from Gupta *et al.* is consistent with this work. The speed data for CCW rotation of the 0.75 μm bead for cells treated with 0 or 2 mM indole are taken from [53], and plotted on top of the PMF-torque curve for the 0.75 μm bead from Fig. 2B.

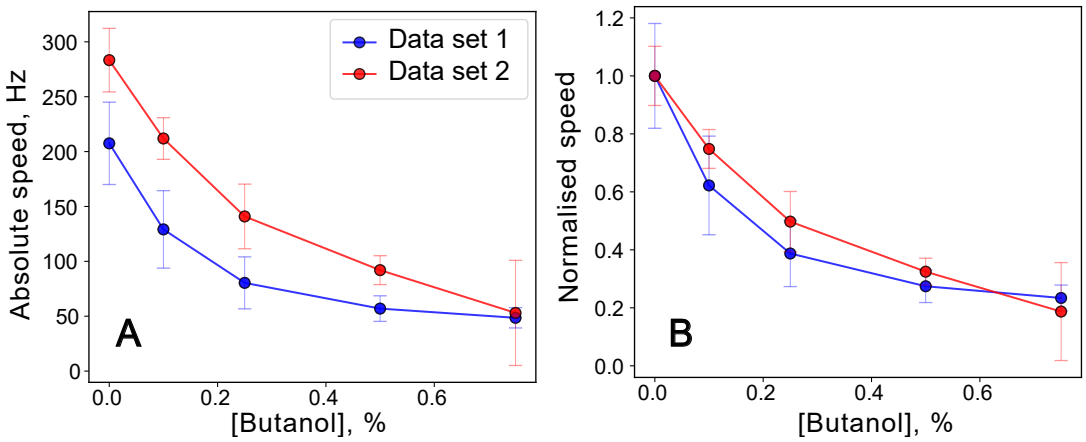

SI Fig. 8. Absolute motor speed can vary between the data sets (A) An example of two data sets collected with 0.5 μm beads that are particularly different in absolute numbers. Despite the difference, the shape of the normalised butanol-speed curves remains unchanged (B). Data points show mean with the standard deviation.

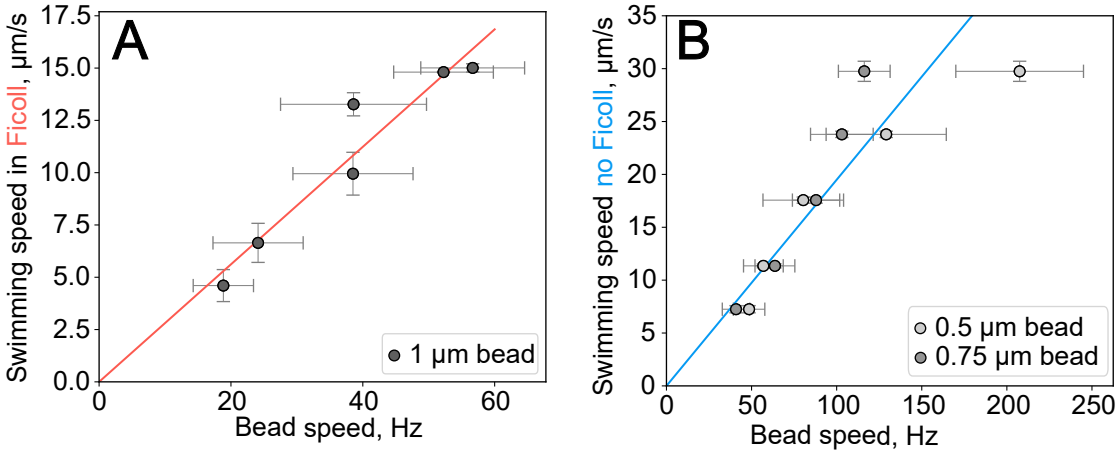

SI Fig. 9 A. Swimming speed in MM9+20 mM glucose media with 8% Ficoll added plotted against the motor speed loaded with 1 μm bead, at the corresponding butanol concentrations. The two speeds are linearly proportional, although the torque is saturated, which indicates that the viscous loads on the motors are equivalent. **B.** Swimming speed in MM9+20 mM glucose media plotted against the motor speed loaded with 0.5 or 0.75 μm bead, at the corresponding butanol concentrations. Neither of the two viscous loads is fully linear with the swimming speed indicating that the equivalent load lies between the two, consistent with our 0.6 μm bead estimate Bead colour coding is the same as in the main text for both (A) and (B). Data points show mean with the standard deviation.

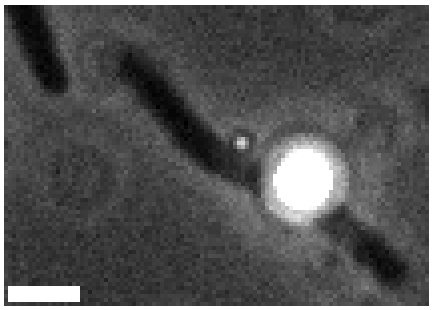

SI Video 1 A cephalexin-treated cell in MM9+20 mM glucose with two beads ($0.5\,\mu\mathrm{m}$ and $1.5\,\mu\mathrm{m}$), each attached to a flagellar motor. The speed of the small bead was measured using this video, and the speed of the large bead was measured using a second video recorded immediately after this one, in which the large bead is in focus. The small bead rotates at $219\,\mathrm{Hz} \pm 19\,\mathrm{Hz}$, and the large bead rotates at $19\,\mathrm{Hz} \pm 2\,\mathrm{Hz}$. Video was slowed down 40x. Scale bar: $2\,\mu\mathrm{m}$.

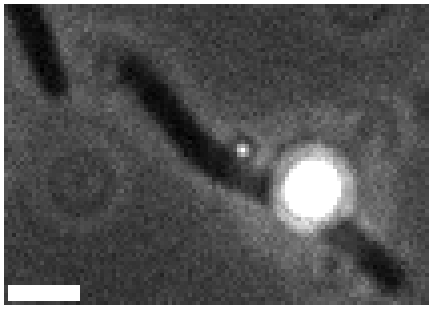

SI Video 2 The same cell as in Video 1, now exposed to 0.5% butanol in MM9+20 mM glucose. The speed of the small bead was measured using this video, and the speed of the large bead was measured using a second video recorded immediately after this one, in which the large bead is in focus. The small bead rotates at $93\,\mathrm{Hz} \pm 3\,\mathrm{Hz}$, and the large bead rotates at $19\,\mathrm{Hz} \pm 1\,\mathrm{Hz}$. Video was slowed down 40x. Scale bar: $2\,\mu\mathrm{m}$.

Supplementary Material Text.

Motor speed variations. The data included in this work were collected in multiple labs by multiple researchers. When accounted for the variations in bead sizes (see SI Table 1), rotation radii (0.1-0.2 μm for smaller beads, 0.2-0.3 μm for larger beads), temperature (19-23°C), or culture OD (2.0-2.6) there is still some unaccounted variability in measured speeds for 1.5 μm in diameter beads. We note, that when accounting for variability based on temperature differences we used estimates based on a chimeric motor, where the stator units are powered by sodium [52]. While these differences do not affect our two main conclusions as illustrated in SI Fig. 8, they affect our estimates of the maximum torque.

Viscosity measurements. Diffusion coefficients obtained from DDM analysis for $0.5\,\mu\mathrm{m}$ and $1\,\mu\mathrm{m}$ beads with and without 8% Ficoll (see *Materials and Methods*) were converted to viscosity values using the Stokes–Einstein–Sutherland equation: $\eta = \frac{k_\mathrm{B}T}{6\pi r_\mathrm{b} D}$, where η is the unknown viscosity, k_B the Boltzmann constant, T the temperature, r_b the bead radius and D the diffusion coefficient measured via DDM.
As a control, we first calculated the viscosity of pure water ($1\,\mathrm{mPa\,s}$) and obtained $\eta_\mathrm{w} = 0.93 \pm 0.01\,\mathrm{mPa\,s}$ and $\eta_\mathrm{w} = 0.85 \pm 0.01\,\mathrm{mPa\,s}$ with $0.5\,\mu\mathrm{m}$ and $1\,\mu\mathrm{m}$ beads respectively. In 8% Ficoll, we obtained $\eta_\mathrm{F} = 3.39 \pm 0.02\,\mathrm{mPa\,s}$ and $\eta_\mathrm{F} = 2.84 \pm 0.02\,\mathrm{mPa\,s}$ with the same bead sizes. Given the systematic deviation from the expected value for water at room temperature, we decided to base our analysis on the relative viscosity increase caused by the addition of 8% Ficoll, the average value of which was $\frac{\eta_\mathrm{F}}{\eta_\mathrm{w}} = 3.49$ when considering both bead sizes.

Equivalent load estimates. Since swimming in 8% Ficoll shows a speed response to butanol treatment identical to that of a $1\,\mu\mathrm{m}$ bead in a bead assay conducted without Ficoll, main text Figure 3B and SI Fig. 9, we conclude that the swimming load in 8% Ficoll corresponds to the load produced by the $1\,\mu\mathrm{m}$ in diameter bead ($r_\mathrm{b,F} = 0.5\,\mu\mathrm{m}$). To determine the equivalent bead size of the swimming load in pure medium (no Ficoll) we re-arrange equations 3 and 4 to solve it for $r_\mathrm{b,w}$:

$$8\pi {r_\mathrm{b,w}}^3 + 6\pi r_\mathrm{b,w} {r_\mathrm{r}}^2 = \frac{\eta_\mathrm{w}}{\eta_\mathrm{F}}\left[8\pi {r_\mathrm{b,F}}^3 + 6\pi r_\mathrm{b,F} {r_\mathrm{r}}^2\right] - \frac{f_\mathrm{f}}{\eta_\mathrm{w}}\left[1 - \frac{\eta_\mathrm{w}}{\eta_\mathrm{F}}\right], \tag{5}$$

with f_f the friction coefficient on the filament stub defined in the main text, $\frac{\eta_\mathrm{F}}{\eta_\mathrm{w}} = 3.49$ measured in experiments, and $\eta_\mathrm{w} = 0.95\,\mathrm{mPa\,s}$. The result is $d_\mathrm{b} = 2r_\mathrm{b} = 0.6\,\mu\mathrm{m}$, consistent with the experiments main text Figure 3A and SI Fig. 9B.

Speed estimates for passive rotation of tethered cells. In Gabel and Berg's study [27], it was assumed that the speeds of two active motors were recorded simultaneously, with one motor driving the rotation of a $0.4\,\mu\mathrm{m}$ in diameter bead and another motor driving the rotation of the tethered cell. Here, we consider a possible scenario that we proposed in the main text, in which the cell is tethered to the slide via a broken motor or a hydrophobic patch on its outer surface [49], which would allow passive rotation of the cell body.
For simplicity we consider that the rotations of the bead and cell body occur about the same axis, a reasonable assumption since detection of body and bead rotations required alignment with a single pinhole in those experiments. Then, the torque-free condition reads $T_\mathrm{b} + T_\mathrm{cell} = 0$, with T_b and T_cell the torques acting on the bead and the cell body, respectively. From this we obtain $\omega_\mathrm{cell} = -\frac{f_\mathrm{b}}{f_\mathrm{cell}}\omega_\mathrm{b}$, with ω_cell and ω_b the respective angular velocities of the cell and bead, and f_cell and f_b the respective rotational friction coefficients.
To estimate the rotational friction coefficient of cells, we use $f_\mathrm{cell} = \frac{8}{3}\frac{\pi\eta a^3}{\ln(2a/b) - 0.5}$ [74], with $2\,\mu\mathrm{m} < 2a < 4\,\mu\mathrm{m}$ and $b = 0.45\,\mu\mathrm{m}$ [74]. We estimate the friction coefficient of the bead as described in *Materials and Methods* of the main text, with $r_\mathrm{b} = 0.2\,\mu\mathrm{m}$, $r_\mathrm{r} = 0.2\,\mu\mathrm{m}$ (lower bound in Gabel and Berg's experiments [74]), and $f_\mathrm{f} = 0.1\,\mathrm{pN\,nm\,rad^{-1}\,s}$.
A passive body counter-rotation speed is then 1-5.5 Hz for a bead rotating at 100 Hz and 2-11 Hz for a bead rotating at 200 Hz, depending on cell size, and in agreement with the values observed in Gabel and Berg's experiment. And, the speeds will vary linearly with the small bead rotation speed as per the torque balance equation.
In the estimates above we neglected any additional friction at the tethering point, and the proximity of the glass slide, as we do not think these affect our estimates (whose upper bounds are already higher than the measured frequencies). We note that the passive rotation case should be distinguishable from the active case in experiments because the former should lead to the bead and body rotating in opposite directions, while the latter should lead to rotations in the same direction. However, since the bead rotation is too fast to be resolved by the eye, it is possible that the two rotations were assumed to be in the same direction, where they were not.